Research Article Vol. 13, No. 2 / 1 Feb 2023 / Optical Materials Express 458

Optical Materials EXPRESS

SiN foundry platform for high performance visible light integrated photonics

JACK A. SMITH,[1,*] HENRY FRANCIS,[2] GABRIELE NAVICKAITE,[2] AND MICHAEL J. STRAIN[1]

[1] *Institute of Photonics, Dept. of Physics, 99 George St., Technology and Innovation Centre, University of Strathclyde, Glasgow G1 1RD, UK*
[2] *LIGENTEC, EPFL Innovation Park, Bâtiment L, Chemin de la Dent d'Oche 1B, 1024 Ecublens, Switzerland*
[*] *jack.smith@strath.ac.uk*

Abstract: We present a high performance silicon nitride photonic integrated circuit platform operating at visible wavelengths, accessible through the commercial foundry, LIGENTEC. Propagation losses were measured across the visible spectrum from 450 nm to 850 nm. For wavelengths above 630 nm, losses were <1 *dB*/*cm* in TE and <0.5 *dB*/*cm* in TM. Additionally, sets of single mode waveguide-coupled ring resonators across three separate chips were tested and analysed. A peak intrinsic Q factor of 3.69×10^6 was measured for a single resonance at ~635.3 nm, with an average value of 2.28×10^6 recorded over 10 peaks in a 3 nm tuning range. Analyses of the loss and coupling, as functions of bus-ring coupling gap and waveguide width, are also presented. High confinement, low loss devices realised on the chip-scale in a wide-bandgap material like silicon nitride are increasingly important for the next generation of integrated optical devices operating at visible wavelengths.

1. Introduction

Mature fabrication processes, low waveguide losses, and tight mode confinement have ensured the widespread adoption of silicon on insulator (SOI) for infrared integrated optics [1,2]. The highly reproducible wafer-scale production of SOI photonic integrated circuits (PICs) offered by commercial silicon foundries gives researchers a quick and inexpensive route towards realizing their own high performance PIC desings, to the great benefit of a number of technologies [3,4]. However, silicon's narrow bandgap (1.1 eV) precludes operation at wavelengths below 1 μm; a region of the electromagnetic spectrum where applications ranging from optical atomic clocks [5,6] to quantum information processing [7,8] could benefit from the enhanced stability and scalability offered by photonic integration [9,10].

Silicon nitride (SiN) has emerged as the leading candidate to extend integrated optics to shorter wavelengths, facilitated by its wide bandgap (5.1 eV), broad transparency window (400-2350 nm), respectable nonlinear refractive index ($n_2 = 2.5 \times 10^{-15}$ [11]), and low optical losses (<0.01 dB/cm at 700 nm [12]). While other materials may have transparency windows extending to even shorter wavelengths (e.g amorphous alumina oxide [13–15], aluminium nitride [16], or tantalum pentoxide [17]), only SiN benefits from mature fabrication processes that allow foundry-scale production of low-loss PICs on large area wafers [18–22].

In this work we present high confinement SiN waveguides and ring resonators (hereafter referred to as *rings*), fabricated and provided by the SiN foundry, LIGENTEC. Delay lines for propagation loss measurements were characterized at wavelengths of 450 nm, 520 nm, 630 nm, 750 nm, and 850 nm. Rings, meanwhile, were characterized with a laser continuously tunable over the 635–638 nm range. Six chips in all were tested: three delay line chips and three ring

#479871 https://doi.org/10.1364/OME.479871
Journal © 2023 Received 17 Nov 2022; revised 12 Jan 2023; accepted 12 Jan 2023; published 24 Jan 2023

chips. A TE mode propagation loss <1 dB/cm at around 635 nm was measured by both the cutback method and extractions of loss from ring resonance fitting. TM losses were found to be lower, at <0.5 dB/cm. For TM polarisation, a peak intrinsic quality (Q) factor of 3.69×10^6 was measured, corresponding to a single distributed ring loss of just 0.19 dB/cm. For singular device applications, this is an exceptional result, given these rings feature high mode confinement factors and comparatively small bend radii [12]. In comparison to multimode SiN disks presented at around this wavelength [23], the use of single mode rings will simplify nonlinear processes like Kerr microcomb generation; not only because of the simplified spectra, but also because of the guarantee of strong overlap in the ring waveguide between the interacting optical modes [24]. Detailed analyses of chip performance and device trends with respect to ring waveguide width and coupling gap are presented. In all, 399 resonances were analysed, consisting of 158 in TE and 241 in TM. Such analyses are crucial for the increased implementation of integrated photonic devices for applications outside the transparency window of traditional PIC foundry materials.

2. Fabrication and methods

The chips were fabricated as part of a LIGENTEC multi-project wafer run. The cladding thickness above and below the SiN is 3.3 µm and 4 µm, respectively. The LIGENTEC AN150 platform, with a SiN thickness of 150nm, was used to address the whole visible wavelength range with possibility to have single mode propagation across this region.

Finite difference eigenmode (FDE) simulations are shown in Fig. 1, with Fig. 1(a) showing the supported modes as a function of width, and Fig. 1(b) showing the electric field magnitude profiles for a selection of three widths used in this work. Given the waveguide's aspect ratio, the fundamental TE mode is better confined than the fundamental TM for a given width. Bend loss simulations were also performed for the two radii used ($r_{ring} = 110\,\mu m$, $r_{delay} = 150\,\mu m$). These radii were found to be large enough that additional radiative bend losses were negligible across the wavelengths, widths, and polarisations featured in this work.

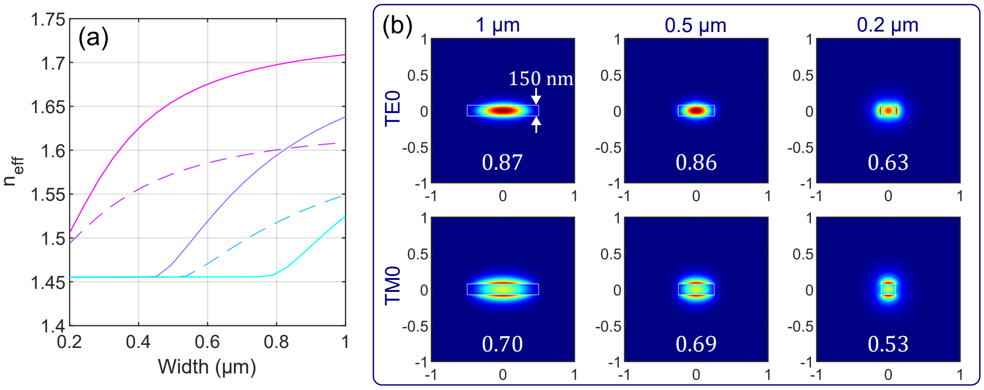

Fig. 1. FDE simulations at λ = 635 nm. (a) Modal effective indices for increasing waveguide width and fixed thickness of 150 nm. Solid (dashed) lines denote TE (TM) polarisations. (b) Fundamental mode profiles for both polarisations and three different widths: 1 µm, 0.5 µm, and 0.2 µm. Modes are also labelled with their confinement factors.

Both delay lines for propagation loss measurements and bus-coupled rings were tested with the set-up shown in Fig. 2(a). The free space output of a New Focus Velocity TLB-6704 was passed through a polarization isolator before being launched into polarization maintaining fiber (PMF). This fiber then couples to a second PMF terminated with a lensed tip (OZ Optics), allowing for optical coupling to the on-chip waveguides. Additionally, the fiber was mounted in a rotating holder, so that its linearly polarised output could be rotated into TE or TM polarizations with respect to the waveguides. The opposite facet of the chip was imaged with a 20× microscope objective. The collected light was passed through a polarization beam splitter (PBS) and iris, before focusing on a CMOS camera (Thorlabs DCC1514M-GL) and an amplified silicon photodetector (PDA100A2), via a beam-splitter. The laser was swept continuously from 635 to 638 nm, while the detector synchronously measured the transmitted power. Data was collected with an Agilent MSO6104A0-1GHz oscilloscope. A trinocular microscope mounted above the device allowed for the capture of images during the measurement, such as those in Fig. 2(b,c) of a microring off and on resonance.

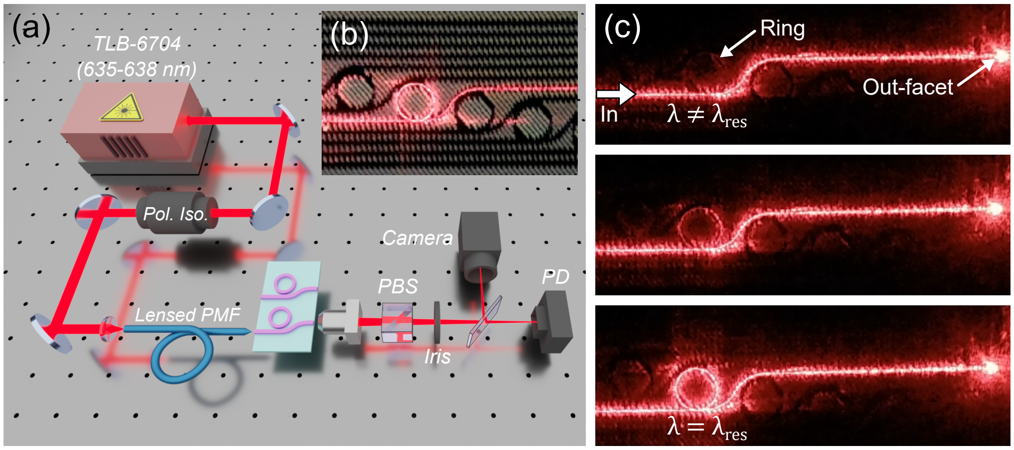

Fig. 2. (a) Optical setup used to take transmission spectra. (b) Image of a portion of an array of rings. (c) Images of a ring coming onto resonance during a wavelength sweep.

3. Delay line propagation loss

To begin, delay lines of increasing length were used to measure the propagation losses for TE polarisation input. Different sources were used to take these measurements over a range of visible wavelengths. Doing so required swapping the tunable TLB-6704 laser with one of a number of fibre-coupled sources commercially available (e.g. Thorlabs LP852-SF30, LP520-SF15, LP450-SF15). Other narrowband components were swapped with their appropriate wavelength equivalents, but the simple nature of the optical set-up essentially allowed for the rapid characterisation of a device over broad wavelength ranges simply by swapping the optical input to the lensed PMF.

The sets of delay lines tested featured lengths ranging from 0.498 cm up to 30.08 cm. The results for a width of 800 nm, averaged over three nominally identical chips, are shown in Fig. 3. For wavelengths of 630 nm and above the traditional cutback method was used to measure insertion loss as a function of guide length. Waveguide propagation loss was calculated from the slope (on a dB scale) of the insertion loss versus delay line length. For wavelengths of 520 nm and below, the extreme path lengths involved weakened the transmitted signal to below the detection limit. However, a measurement could still be made by analysing the vertically scattered light, the intensity of which decays exponentially along any selected length of waveguide propagation. Therefore, vertically scattered light was imaged with a long working distance microscope and CMOS camera. The local intensity of the optical mode in the waveguide is assumed to be linearly related to the scattered light collected. Local scattering around the waveguide was measured in small regions of interest to average out pixel to pixel variations. The integrated intensity in these regions of interest were then plotted as functions of length along the delay line, as in Fig. 3(a). Since the longer wavelengths could traverse the full length of the delay line, both the inward and outward directions of the spiral were illuminated. This limited the ability to resolve sections of waveguide to integrate the vertically scattered intensity over, and prevented a comparative measurement of the two methods.

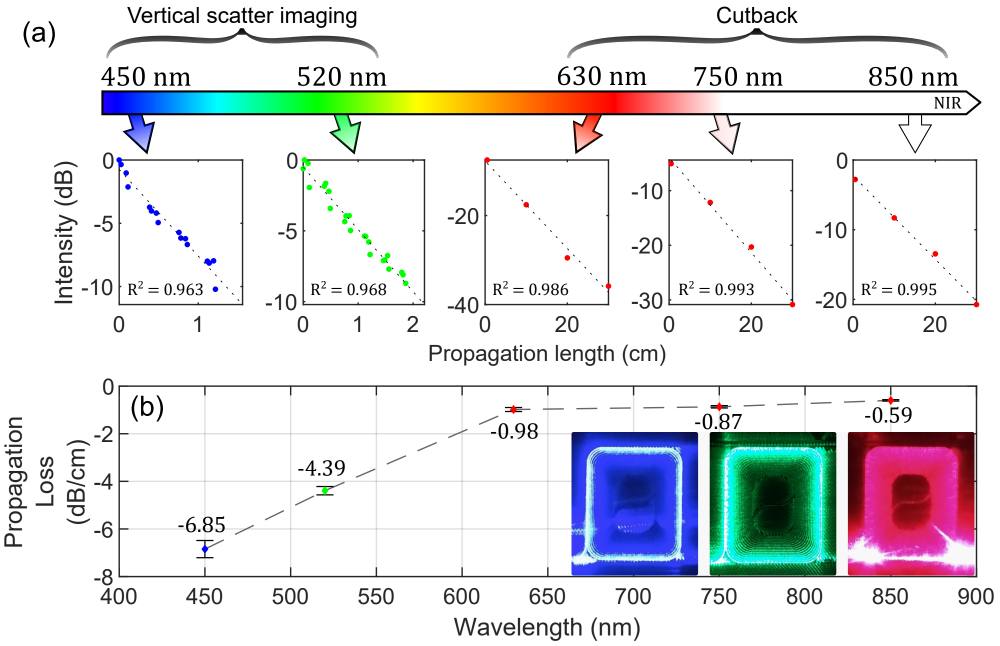

Fig. 3. (a) Individual propagation loss measurements, averaged over three chips, taken across the visible spectrum. (b) Propagation loss values, extracted from the slopes of the line fits above, with error bars denoting one standard error in the slope estimate.

The slopes of the straight line fits in Fig. 3(a) are the data points in Fig. 3(b), which also features some top-down images of the illuminated delay lines during the measurement process. Losses are $<1\ dB/cm$ for wavelengths $>600\ nm$, but increase towards the blue end of the spectrum. Although relatively high, similar losses at shorter wavelengths have been noted in SiN guides of similar dimensions [25,26]. These losses can be mitigated by optimising the waveguide geometry – by either increasing its bend radius from its present value of 150 µm, or increasing the width beyond 800 nm. Furthermore, future designs could feature delay lines of shorter overall length, so that a cutback measurement could be made to verify these results in the shorter wavelengths.

4. Ring resonator transmission

Separate chips, featuring sets of evanescently side-coupled all-pass ring resonators were then measured using a laser source tunable over 635–638 nm, as shown in Fig. 2. Both the waveguide width and coupling gap were varied. Transmission spectra showed combs of modes characteristic of single mode rings, even for those widths which according to Fig. 1(a) support weakly confined higher order modes. Resonance lineshapes were fitted with the well-known notch-filter transmission function [27]:

$$T_n = \frac{a^2 + r^2 - 2racos(\phi)}{1 + (ra)^2 - 2racos(\phi)}, \tag{1}$$

where a is the single-pass field amplitude transmission in the ring ($a = 1$ for a lossless ring), from which the distributed loss α can be calculated and expressed in units of dB/cm. r is the bus waveguide's self-coupling coefficient, which (for lossless coupling) is related to the power cross-coupling, κ, through $\kappa = 1 - r^2$. Loss in the coupling section is therefore contained in the parameter a. The single-pass phase shift in the ring, ϕ, relates to the propagation constant β through $\phi = \beta L$, where L is the cavity length. The free parameters a and r, which enter Eq. (1) symmetrically and would otherwise be indistinguishable, can in the present case be disentangled by inspecting trends in the coupling with respect to gap and waveguide width [28]. Critical-coupling occurs when $r = a$, under-coupling when $r>a$, and over-coupling when $r<a$. The loaded Q factor, Q_L, can be written as the following function of these parameters [27]:

$$Q_L = \frac{\pi n_g L \sqrt{ra}}{\lambda_r (1 - ra)}, \tag{2}$$

where λ_r is the resonant wavelength, L is the cavity length, and n_g is the group index, given by [27]:

$$n_g = n_{eff} - \lambda_0 \frac{dn_{eff}}{d\lambda} = \frac{\lambda^2}{FSR \times L}, \tag{3}$$

with FSR the free-spectral range. Finally, the intrinsic Q factor is given simply by [16]:

$$Q_{int} = \frac{2Q_L}{1 \pm T_0^{1/2}}, \tag{4}$$

where T_0 is the normalised on-resonance transmission, and the summation or subtraction in the denominator is taken in the case of under-coupling and over-coupling respectively.

4.1. TE performance

Figure 4 shows two spectra and exemplary resonance fits on those dips labelled with red arrows. These measurements were made for TE input. Figs. 4(a,b) correspond to an under-coupled ring of waveguide width of 1 µm, while Figs. 4(c,d) correspond to a near critically coupled ring of width of 0.5 µm. The coupling gap for both was nominally constant, at 300 nm. The respective loaded (intrinsic) Q factors of the resonances in Fig. 4(b) and (d) are 1.56×10^6 (1.67×10^6) and 2.20×10^5 (4.40×10^5).

These represent some of the narrowest and deepest resonances measured for a TE polarisation. TM resonances with narrower *intrinsic* linewidths will be detailed later. A selection of representative TE lineshapes for different widths are overlaid in Fig. 5, and clearly show a trend toward critical coupling for a waveguide width of 500 nm. Narrower guides were over-coupled, and increasingly wider guides were increasingly under-coupled, featuring a monotonic decrease in linewidth and extinction.

Irrespective of coupling, a change in width will also change the ring loss and intrinsic Q_{int} factor. These statistics are plotted in Fig. 6, where Fig. 6(a) shows results from a single chip, and Fig. 6(b) shows results from all three chips. Note the minimum loss for a width of 800 nm is in agreement with earlier propagation loss measurements at 630 nm on guides of the same geometry. The slight increase in loss overall can be attributed to additional loss sources contained in a ring's distributed loss, such as loss in the coupling section [27]. From a single fit (shown in Fig. 4(b)), the best Q_{int} and distributed loss values at TE are 1.67×10^6 and 0.49 dB/cm, with the averages over the six resonances in that spectrum being 9.79×10^5 and 0.94 dB/cm. Finally, the power cross-coupling is well modelled by a simple exponential fit, as in Fig. 6, reflecting the dependence of the coupling on the exponentially decaying evanescent tails in the bus and ring waveguides.

4.2. TM performance

Analysis of the rings for TM begins in a similar fashion, with the waterfall plot shown in Fig. 7. Unlike the TE case, this first set of TM results are entirely over-coupled – evident in the trends of

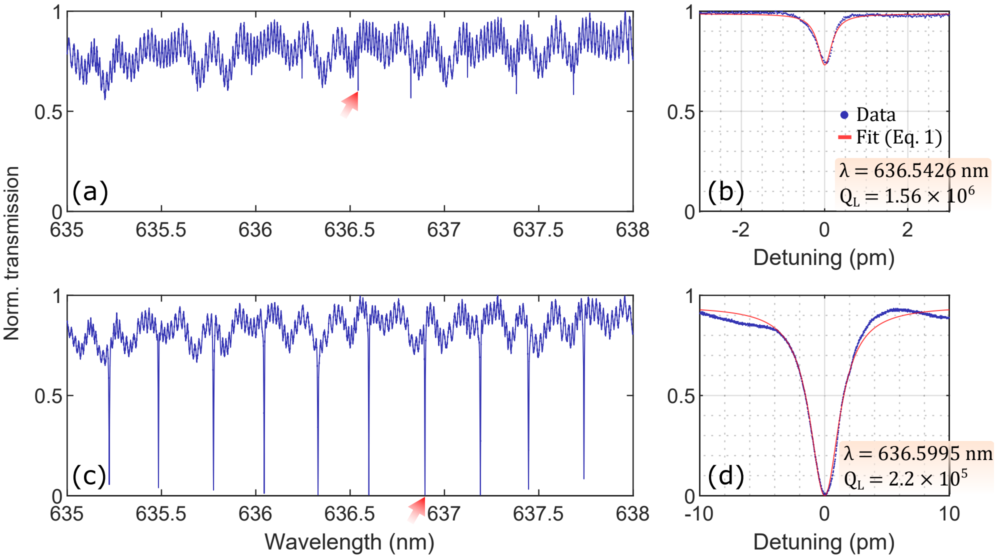

Fig. 4. (a) Under-coupled ring transmission, ($width = 1\,\mu m$, $gap = 300\,nm$). (b) Fit on resonance dip labelled by red arrow in previous, with loaded Q_L shown. (c) Critically coupled ring transmission, ($width = 0.5\,\mu m$, $gap = 300\,nm$) (d) Fit on resonance dip labelled by red arrow in previous.

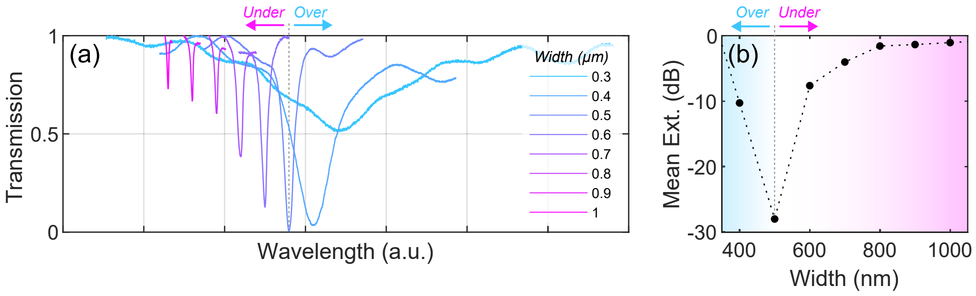

Fig. 5. (a) Typical TE lineshapes for different waveguide widths and a fixed gap of 300 nm. Critical coupling is observed for a width of 500 nm. (b) Mean extinction values for fitted peaks in each width's corresponding spectra.

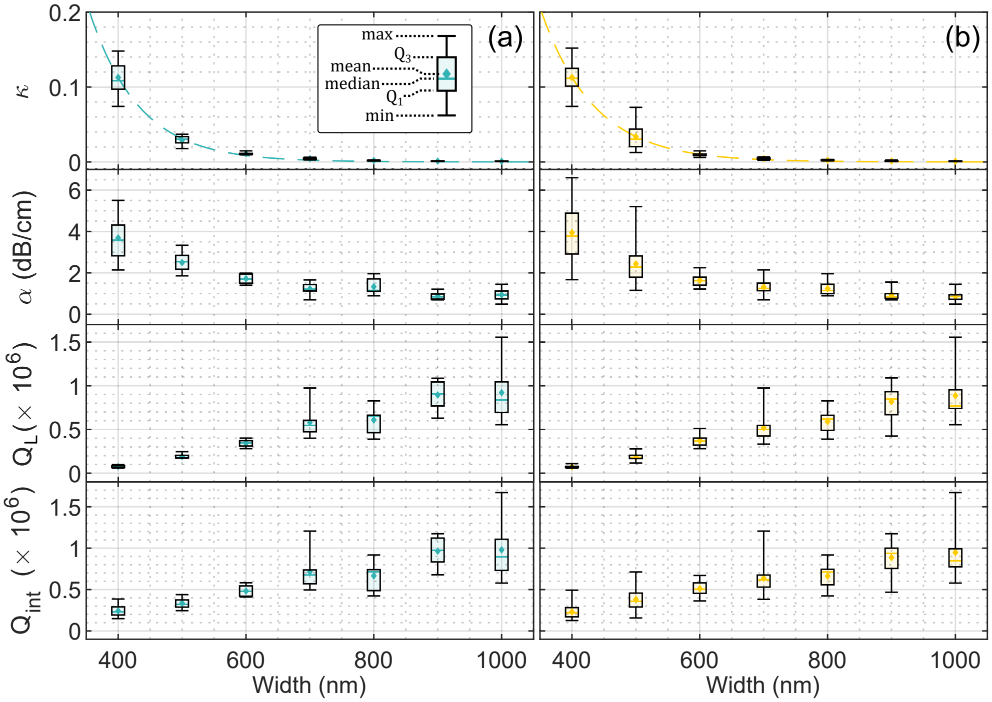

Fig. 6. (a) Boxplots of extracted fit parameters for one chip at TE, $g = 300\,nm$. (b) The same, for all three chips and 158 resonances in total.

the example lineshapes in Fig. 7(a), the absence of a sharp increase in mean extinction in Fig. 7(b), and the fact that extracted power cross-coupling values are well modelled by an exponentially decaying function (Fig. 8). It may be argued that there exists an intermediate waveguide width for which the coupling would be critical. However, if this were the case, then the wider guides would be under-coupled if nominal trends were maintained. If, for example, a width of 1 µm was in fact under-coupled, there would be a sharp decrease in Q_{int} that would reverse the trend shown in Fig. 8. Presently, the best average Q_{int} is 2.32×10^6, measured for a width of 1 µm. In the under-coupled case, according to Eq. (4), this would reduce to 7.73×10^5. Given both the unlikelihood of this trend reversal, and the steady increase in mean extinction for decreasing width, we can be confident these TM resonances are all over-coupled.

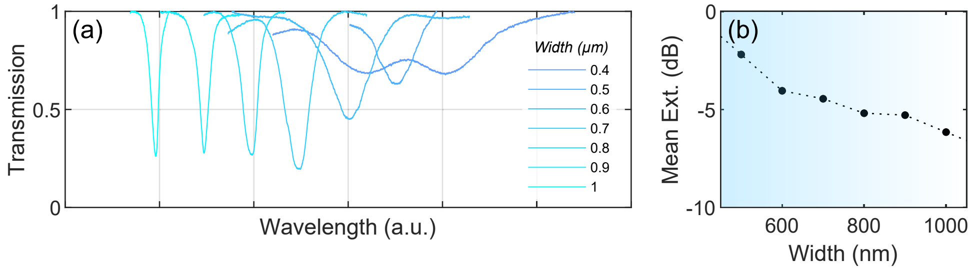

Fig. 7. (a) Typical TM lineshapes for different waveguide widths and a fixed gap of 300 nm. (b) Mean peak extinctions.

With this in mind, we note an extremely high Q resonance, shown in Fig. 9, which was taken for the same device whose TE transmission is shown in Fig. 4(a) – a width of 1 µm and gap of

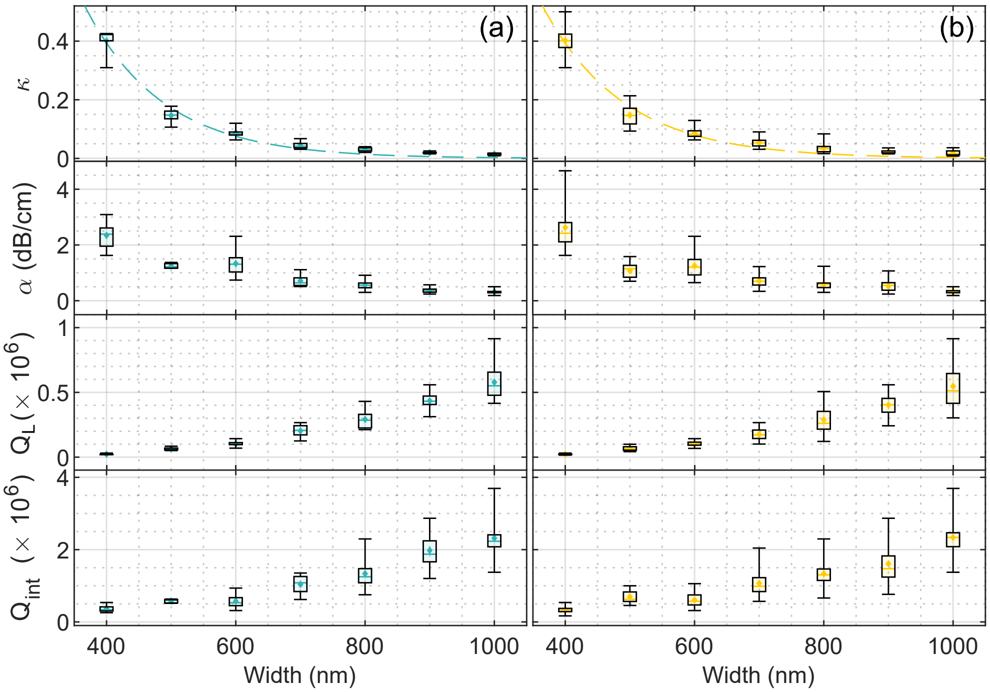

Fig. 8. (a) Boxplots of extracted fit parameters for one chip at TM, $g = 300\,nm$. (b) The same, for all three chips and 167 resonances in total.

300 nm. As expected, the loaded Q_L is lower than the under-coupled TE case, at 9.14×10^5. However, an exceptionally low distributed loss of 0.19 dB/cm gives this TM resonance a Q_{int} of 3.69×10^6. This is the highest value recorded in literature in this wavelength range for high confinement rings, to the best of our knowledge. Over all the resonances shown in Fig. 9(a), mean Q_{int} and α values of 2.28×10^6 and $0.32\,dB/cm$ are measured. For a width of 1 µm, of the 28 resonances measured over 3 identical chips, 20 had a Q_{int} in excess of 2×10^6. While both polarisations offer $<1\,dB/cm$ of ring loss, an improved performance for TM is likely due to the difference in mode profiles, and the reduction in confinement to the SiN core evident in Fig. 1(b).

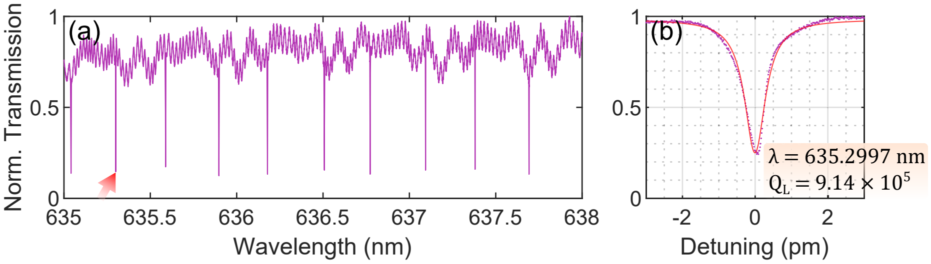

Fig. 9. (a) TM transmission spectra, ($width = 1\,\mu m$, $gap = 300\,nm$). (c) Fit on the resonance labelled, with peak Q_{int} of 3.69×10^6.

Finally, since for the original gap of 300 nm the rings start out over-coupled for TM, it is logical to increase this gap and examine trends in device performance in a similar fashion as above. These results are shown in Fig. 10, for two representative widths. An increase in bus-ring separation exponentially decreases the power coupled between the two, until at some separation the coupled power matches the power lost in the ring and critical coupling is achieved. Red circles denote rings either at, or approximately at, critical coupling, demonstrating less lossy rings with wider waveguides require a smaller power cross-coupling fraction to achieve critical coupling ($r = a$). Meanwhile, the loss values (and hence Q_{int}) are exceedingly flat with respect to coupling gap. Even for narrow guides, this flatness is maintained, suggesting no significant dependence on any loss in the point-coupling section between bus and ring. This shows that the coupling gap is an effective way – well within fabrication tolerances – to target critically coupled rings. This method is especially effective for narrower guides whose increased losses push the critical gap to values far from the minimum separation defined by the lithography process. For high Q rings with widths of 1 µm, increased modal confinement and greatly reduced ring losses ($a \approx 1$) mean the gap must be much more gradually changed to attain critical coupling. This is evident in the flattening of the exponential trends in κ for increasing widths in Fig. 10. While such gradual changes may still be within fabrication tolerances, it may be easier to fix the coupling gap at some value and instead use racetrack resonator structures. The power cross-coupling can then be marginally increased by laterally offsetting the racetrack with respect to the bus waveguide, reducing the effective coupling length between the parallel sections of bus and racetrack waveguides.

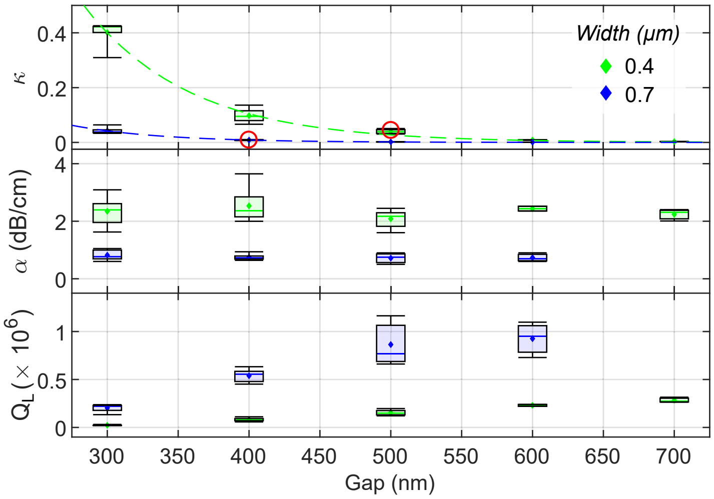

Fig. 10. (a) Boxplots of extracted fit parameters for one chip at TM for increasing gap, two waveguide widths, and 74 resonances in total. Red circles denote those geometries which are critically coupled.

5. Conclusion

We have presented a detailed analysis of a commercially available SiN platform operating at visible wavelengths. Typically, exceptionally high Q factors come at the cost of decreased confinement, large bend radii, and increased device footprint. Here we have shown record Q factors of 3.69×10^6, in a single mode ring with a radius of just 110 µm and width 1 µm – useful, for example, in applications of visible light soliton microcomb generation [29] and chip-scale optical parametric oscillators [30]. More generally, our systematic analysis over three chips and 399 resonances has shown device results which are highly reproducible and with low errors. For example, losses are sustained at levels below 1 dB/cm for widths of 1 µm at TE, and below 0.5 dB/cm for TM. The availability of such a foundry-accessible platform for PICs transparent to visible wavelength represents an important advancement in the broadening of integrated optics to include those applications not traditionally applicable to silicon photonics.

Funding. Royal Academy of Engineering (Research Chairs and Senior Research Fellowships); Engineering and Physical Sciences Research Council (EP/R03480X/1, EP/V004859/1); Innovate UK (50414); Horizon 2020 Framework Programme (898074 (POTION)).

Acknowledgments. This work was funded by the Royal Academy of Engineering (Research Chairs and Senior Research Fellowships), Engineering and Physical Sciences Research Council (EP/R03480X/1, EP/V004859/1) and Innovate UK (50414). Author G. N. acknowledges funding from the European Union's Horizon 2020 research and innovation programme under the Marie Sklodowska-Curie grant agreement No 898074 (POTION).

Disclosures. The authors declare no conflicts of interest.

Data availability. All data underpinning this publication are openly available from the University of Strathclyde KnowledgeBase [31].

References

1. R. A. Soref and J. P. Lorenzo, "Single-crystal silicon: a new material for 1.3 and 1.6 μm integrated-optical components," Electron. Lett. **21**(21), 953–954 (1985).
2. N. Margalit, C. Xiang, S. M. Bowers, A. Bjorlin, R. Blum, and J. E. Bowers, "Perspective on the future of silicon photonics and electronics," Appl. Phys. Lett. **118**(22), 220501 (2021).
3. B. Jalali and S. Fathpour, "Silicon photonics," J. Lightwave Technol. **24**(12), 4600–4615 (2006).
4. D. Thomson, A. Zilkie, J. E. Bowers, T. Komljenovic, G. T. Reed, L. Vivien, D. Marris-Morini, E. Cassan, L. Virot, J. M. Fédéli, J. M. Hartmann, J. H. Schmid, D. X. Xu, F. Boeuf, P. O'Brien, G. Z. Mashanovich, and M. Nedeljkovic, "Roadmap on silicon photonics," J. Opt. **18**(7), 073003 (2016).
5. A. P. Vandevender, Y. Colombe, J. Amini, D. Leibfried, and D. J. Wineland, "Efficient fiber optic detection of trapped ion fluorescence," Phys. Rev. Lett. **105**(2), 023001 (2010).
6. A. D. Ludlow, M. M. Boyd, J. Ye, E. Peik, and P. O. Schmidt, "Optical atomic clocks," Rev. Mod. Phys. **87**(2), 637–701 (2015).
7. G. Moody, L. Chang, and T. J. Steiner, "Chip-scale nonlinear photonics for quantum light generation," AVS Quantum Sci. **2**(4), 041702 (2020).
8. N. H. Wan, T. J. Lu, K. C. Chen, M. P. Walsh, M. E. Trusheim, L. De Santis, E. A. Bersin, I. B. Harris, S. L. Mouradian, I. R. Christen, E. S. Bielejec, and D. Englund, "Large-scale integration of artificial atoms in hybrid photonic circuits," Nature **583**(7815), 226–231 (2020).
9. D. J. Blumenthal, R. Heideman, D. Geuzebroek, A. Leinse, and C. Roeloffzen, "Silicon Nitride in Silicon Photonics," Proc. IEEE **106**(12), 2209–2231 (2018).
10. D. J. Blumenthal, "Photonic integration for UV to IR applications," APL Photonics **5**(2), 020903 (2020).
11. K. Ikeda, R. E. Saperstein, N. Alic, and Y. Fainman, "Thermal and Kerr nonlinear properties of plasma-deposited silicon nitride/silicon dioxide waveguides," Opt. Express **16**(17), 12987–12994 (2008).
12. N. Chauhan, J. Wang, D. Bose, K. Liu, R. L. Compton, C. Fertig, C. W. Hoyt, and D. J. Blumenthal, "Ultra-low loss visible light waveguides for integrated atomic, molecular, and quantum photonics," Opt. Express **30**(5), 6960 (2022).
13. M. M. Aslan, N. A. Webster, C. L. Byard, M. B. Pereira, C. M. Hayes, R. S. Wiederkehr, and S. B. Mendes, "Low-loss optical waveguides for the near ultra-violet and visible spectral regions with Al_2O_3 thin films from atomic layer deposition," Thin Solid Films **518**(17), 4935–4940 (2010).
14. J. Mu, M. Dijkstra, J. Korterik, H. Offerhaus, and S. M. García-Blanco, "High-gain waveguide amplifiers in Si_3 N_4 technology via double-layer monolithic integration," Photonics Res. **8**(10), 1634 (2020).
15. W. A. Hendriks, L. Chang, C. I. van Emmerik, J. Mu, M. de Goede, M. Dijkstra, and S. M. Garcia-Blanco, "Rare-earth ion doped Al_2O_3 for active integrated photonics," Adv. Phys.: X **6**(1), 1 (2021).
16. T. J. Lu, M. Fanto, H. Choi, P. Thomas, J. Steidle, S. Mouradian, W. Kong, D. Zhu, H. Moon, K. K. Berggren, J. Kim, M. Soitani, S. Preble, and D. Englund, "Aluminum nitride integrated photonics platform for the ultraviolet to visible spectrum," Opt. Express **26**(9), 11147 (2018).
17. M. Belt, M. L. Davenport, J. E. Bowers, and D. J. Blumenthal, "Ultra-low-loss Ta_2O_5-core/SiO_2-clad planar waveguides on Si substrates," Optica **4**(5), 532–536 (2017).
18. J. Faneca Ruedas, J. Sabek, T. Dominguez Bucio, F. Y. Gardes, and C. Dominguez Horna, "Basic building blocks development for a SiN platform in the visible range," in *IEEE International Conference on Group IV Photonics GFP*, vol. 2021-Decem (IEEE Computer Society, 2021).
19. M. Lelit, M. Słowikowski, M. Filipiak, M. Juchniewicz, B. Stonio, B. Michalak, K. Pavłov, M. Myśliwiec, P. Wiśniewski, A. Kaźmierczak, K. Anders, S. Stopiński, R. B. Beck, and R. Piramidowicz, "Passive photonic integrated circuits elements fabricated on a silicon nitride platform," Materials **15**(4), 1398 (2022).
20. V. S. S. Sundaram, E. Manfreda-Schulz, T. H. Stievater, N. F. Tyndall, T. Palone, V. Deenadayalan, C. Tison, Z. Smith, D. Hucul, G. A. Howland, M. L. Fanto, and S. F. Preble, "Highly-confined, low-loss visible photonics using foundry-fabricated silicon nitride circuits," in *Optics InfoBase Conference Papers*, (Optica Publishing Group, 2022), p. JTh3B.14.

21. Y. Bian, C. Meagher, and K. Nummy, *et al.*, “Monolithically integrated silicon nitride platform,” in *Optical Fiber Communication Conference*, (Optica Publishing Group, 2021), pp. Th1A–46.
22. P. Mu noz, P. W. van Dijk, D. Geuzebroek, M. Geiselmann, C. Dominguez, A. Stassen, J. D. Doménech, M. Zervas, A. Leinse, C. G. Roeloffzen, B. Gargallo, R. Ba nos, J. Fernández, G. M. Cabanes, L. A. Bru, and D. Pastor, “Foundry developments toward silicon nitride photonics from visible to the mid-infrared,” IEEE J. Sel. Top. Quantum Electron. **25**(5), 1–13 (2019).
23. E. S. Hosseini, S. Yegnanarayanan, A. H. Atabaki, M. Soltani, and A. Adibi, “High quality planar silicon nitride microdisk resonators for integrated photonics in the visible wavelength range,” Opt. Express **17**(17), 14543–14551 (2009).
24. L. Chang, S. Liu, and J. E. Bowers, “Integrated optical frequency comb technologies,” Nat. Photonics **16**(2), 95–108 (2022).
25. C. Sorace-Agaskar, S. Bramhavar, D. Kharas, W. Loh, P. W. Juodawlkis, J. Chiaverini, and J. M. Sage, “Multi-layer integrated photonics from the ultraviolet to the infrared,” in *Frontiers in Biological Detection: From Nanosensors to Systems X*, vol. 10510 (SPIE, 2018), pp. 36–45.
26. E. Obrzud, V. Brasch, T. Voumard, A. Stroganov, M. Geiselmann, F. Wildi, F. Pepe, S. Lecomte, and T. Herr, “Visible blue-to-red 10 ghz frequency comb via on-chip triple-sum-frequency generation,” Opt. Lett. **44**(21), 5290–5293 (2019).
27. W. Bogaerts, P. De Heyn, T. Van Vaerenbergh, K. De Vos, S. Kumar Selvaraja, T. Claes, P. Dumon, P. Bienstman, D. Van Thourhout, and R. Baets, “Silicon microring resonators,” Laser Photonics Rev. **6**(1), 47–73 (2012).
28. W. R. McKinnon, D. X. Xu, C. Storey, E. Post, A. Densmore, A. Delâge, P. Waldron, J. H. Schmid, and S. Janz, “Extracting coupling and loss coefficients from a ring resonator,” Opt. Express **17**(21), 18971 (2009).
29. S. H. Lee, D. Y. Oh, Q. F. Yang, B. Shen, H. Wang, K. Y. Yang, Y. H. Lai, X. Yi, X. Li, and K. Vahala, “Towards visible soliton microcomb generation,” Nat. Commun. **8**(1), 1295 (2017).
30. X. Lu, G. Moille, A. Rao, D. A. Westly, and K. Srinivasan, “On-chip optical parametric oscillation into the visible: generating red, orange, yellow, and green from a near-infrared pump,” Optica **7**(10), 1417 (2020).
31. J. Smith, “Data for: a SiN foundry platform for high performance visible light integrated photonics,” University of Strathclyde KnowledgeBase, 2022, https://doi.org/10.15129/6916c846-53b5-43fb-8877-6796e54d43c7.